SIMULATION OF THE EFFECT OF MORTAR-AGGREGATE INTERFACE ON MESO-SCALE DAMAGE BEHAVIOR OF STEEL FIBER-REINFORCED CONCRETE

Hoang-Quan Nguyen¹, Bao-Viet Tran^{01,*}, Gia-Khuyen Le², Thi-Huong-Giang Nguyen³

¹Faculty of Construction Engineering, University of Transport and Communications,

3 Cau Giay street, Dong Da district, Hanoi, Vietnam

²Campus in Ho Chi Minh City, University of Transport and Communications,

No. 450-451 Le Van Viet street, Thu Duc city, Ho Chi Minh city, Vietnam

³Faculty of Basic Sciences, University of Transport and Communications,

3 Cau Giay street, Dong Da district, Hanoi, Vietnam

*E-mail: viettb@utc.edu.vn

Received: 23 January 2025 / Revised: 03 April 2025 / Accepted: 17 April 2025 Published online: 29 May 2025

Abstract. This paper focuses on studying the effect of the interface between the mortar matrix and aggregate particles on the meso-scale behavior of steel fiber-reinforced concrete (SFRC). To achieve this, a phase field model enhanced by a cohesive law is applied to this specific context. Initially, the model is evaluated under a basic scenario with a single aggregate particle embedded in a homogeneous mortar matrix. The influence of interface parameters on various volume fractions of aggregate is examined, considering both the elastic and damage behavior of the material. The main findings are then applied to the meso-scale level of SFRC and compared with experimental results as well as recent models to validate the proposed effects.

Keywords: SFRC, phase field method, damage, crack, interface.

1. INTRODUCTION

Concrete has become the predominant material in construction today, thanks to its many benefits, including affordability and ease of shaping. Despite these advantages, concrete has some drawbacks, such as low tensile strength and high brittleness. To mitigate these issues, steel fibers are added to concrete, resulting in steel fiber-reinforced concrete (SFRC). The integration of steel fibers in the concrete matrix significantly enhances

the composite's ductility, toughness, and energy dissipation capacity [1–3]. The role of the steel fibers becomes crucial after matrix cracking occurs, as they help resist crack propagation. Even after cracking, the fibers maintain some load-bearing capacity, preventing sudden failure of the composite. The application of this material has increased in recent years, making it very attractive for many structures, such as airfields [4], industrial slabs [5], bridges [6], tunnels [7], and many other civil engineering constructions.

The modeling of SFRC behavior has attracted significant attention within the scientific community due to the inherent challenges. Concrete is a quasi-brittle material, and its mechanical properties are greatly influenced by the initiation, growth, and coalescence of microcracks. The addition of steel fibers introduces further complexity to material modeling and complicates the analysis. For steel fiber-reinforced concrete, discrete [8] or semi-discrete [9] fiber treatments are commonly utilized. This approach allows for the observation of fiber distribution and the interaction between fibers and the concrete. However, the complexity of this approach is very high due to the numerous fibers in the concrete matrix, the nonlinear behavior of concrete, and the nonlinear behavior of the fiber-concrete interface.

In [10], we introduced a cohesive law within the phase-field method to model the damage behavior of SFRC. This method effectively simulates crack propagation by employing a scalar variable, ranging from 0 (intact state) to 1 (fully broken state), to represent material degradation. The cohesive law describes the bonding behavior at material interfaces. Using this model, we successfully simulated the three-point bending test of SFRC. However, the original model only considered the interface between fibers and the mortar matrix, assuming a perfect bond between aggregates and the mortar matrix.

This paper revisits the model by incorporating imperfect interfaces for both fiber-mortar and aggregate-mortar interactions. The paper is structured as follows. In Section 2, a phase-field model for interfacial cohesive fracture is briefly summarized. Next, in Section 3, a single circular aggregate embedded in a homogeneous mortar matrix is analyzed to understand how the interface parameters influence the elastic and damage behavior of the specimen. In Section 4, the effects of imperfect interfaces are evaluated by comparing the results with experimental data and recent models of three-point bending tests. Finally, Section 5 presents the conclusions and perspectives of the model.

2. THEORETICAL BASICS

In this section, a phase-field model for interfacial cohesive fracture is briefly summarized. Consider a domain containing three phases: matrix, aggregate, and steel fiber, along with the interfaces between the aggregate and matrix, and between the steel fiber

and matrix. These phases are assumed to behave elastically and are characterized by stiffness $\mathbb{C}(x)$. The brittle fracture behavior and cohesive fracture are described by fracture energy $g_c(x)$ and $G(\llbracket u \rrbracket, \kappa)$, respectively. In a standard framework of sharp discontinuity, the total energy of cracked heterogeneous solids is given by

$$E = \int_{\Omega/\Gamma} \psi^{e}(\mathbf{u}) d\Omega + \int_{\Gamma} g_{c} d\Gamma + \int_{\Gamma_{\beta}} G(\llbracket \mathbf{u} \rrbracket, \kappa) d\Gamma_{\beta}.$$
 (1)

In the regularization framework, the phase-field variable d(x) represents a smeared crack, and $\gamma_d(d, \nabla d)$ denotes the crack density function per unit volume. The interfaces between phases are considered imperfect and are characterized by a cohesive law expressed in Eq. (2)

$$t = \frac{\partial G(\llbracket u \rrbracket, \kappa)}{\partial \llbracket u \rrbracket} \to t = t(\llbracket u \rrbracket, \kappa). \tag{2}$$

The interface is also represented in a smeared sense, characterized by the interface variable $\beta(x)$ and the interfacial energy density function $\gamma_{\beta}(\beta, \nabla \beta)$. To regularize the displacement jump $[\![\mathbf{u}]\!]$, an auxiliary field v(x) is introduced. Consequently, the energy functional is reformulated as

$$E = \int_{\Omega} \left(g(d) \psi^{e}(\boldsymbol{u}, \boldsymbol{v}) + g_{c} \gamma_{d}(d, \nabla d) + G(\boldsymbol{v}, \kappa) \gamma_{\beta}(\beta, \nabla \beta) + \alpha \frac{\partial \boldsymbol{v}}{\partial x_{n}} \cdot \frac{\partial \boldsymbol{v}}{\partial x_{n}} \right) d\Omega, \quad (3)$$

where $\alpha > 0$ ensures that the auxiliary displacement jump field remains constant in the normal direction. The degradation function $g(d) = (1-d)^2 + k$ models the reduction in material strength, with k being a small positive parameter to maintain numerical stability in the fully damaged state. Assuming that the damage is created by traction only, Miehe et al. [11] have proposed a model in which the elastic strain is decomposed into positive ε^+ and negative ε^- parts as follows

$$\varepsilon^e = \varepsilon^{e+} + \varepsilon^{e-},$$
(4)

$$\boldsymbol{\varepsilon}^{e+} = \sum_{i=1}^{D} \left\langle \varepsilon^{i} \right\rangle_{+} \boldsymbol{n}^{i} \otimes \boldsymbol{n}^{i}, \quad \boldsymbol{\varepsilon}^{e-} = \sum_{i=1}^{D} \left\langle \varepsilon^{i} \right\rangle_{-} \boldsymbol{n}^{i} \otimes \boldsymbol{n}^{i}, \tag{5}$$

where ε^i and \mathbf{n}^i are the eigenvalues and eigenvectors of ε^e , satisfying $\varepsilon^e \mathbf{n}^i = \varepsilon^i \mathbf{n}^i$, and $\langle x \rangle_{\pm} = (x \pm |x|)$ /2. Its derivatives with respect to the elastic strain define two projection tensors as

$$\wp^{\pm}\left(\varepsilon^{e}\right) = \partial_{\varepsilon^{e}}\left[\varepsilon^{e\pm}\left(\varepsilon^{e}\right)\right],\tag{6}$$

which are isotropic tensors and nonlinear functions of ε^e , providing the nonlinearity in the mechanical problem.

Therefore, the elastic strain density can be written as

$$\psi^{e}(u,v) = g(d) \psi^{e+}(u,v) + \psi^{e-}(u,v), \qquad (7)$$

$$\psi^{e\pm}\left(u,v\right) = \frac{\lambda}{2} \left[\left\langle \operatorname{Tr}\left(\varepsilon^{e}\right) \right\rangle_{\pm} \right]^{2} + \mu \operatorname{Tr}\left\{ \left(\varepsilon^{\pm}\right)^{2} \right\}, \tag{8}$$

where λ and μ are the Lamé constants.

Applying the maximum dissipation principle and energy minimization to Eq. (2), we obtain the set of coupled equations to determine the phase-field d(x) as follows:

$$\begin{cases}
2(1-d)\mathcal{H} - \frac{g_c}{\ell_d}(d - \ell d^2 \Delta d) = 0, & (\Omega) \\
d(x) = 1, & (\Gamma) \\
\nabla d(x) \cdot \mathbf{n} = 0, & (\partial \Omega)
\end{cases} \tag{9}$$

and the displacement u(x), and the displacement jump v(x)

$$\begin{cases}
\nabla \cdot \sigma (u, v, d) = 0, & (\Omega) \\
u(x) = \overline{u}, & (\partial \Omega_u) \\
\sigma \cdot n = \overline{F}, & (\partial \Omega_F) \\
\gamma_{\beta} (t(v, \kappa) - \sigma \cdot n) = \alpha \frac{\partial v}{\partial x_n} \cdot \frac{\partial v}{\partial x_n}, & (\Gamma_{\beta}) \\
\frac{\partial v (x_c)}{\partial x_n} = 0, & (\partial \Gamma_{\beta})
\end{cases}$$
(10)

In (9), \mathcal{H} is the history strain energy density function, introduced to describe a dependence on history and possible loading-unloading [11]. This function is expressed as follows

$$\mathcal{H}(x,t) = \max_{\tau \in [0,t]} \left\{ \psi^{e+}(x,t) \right\}. \tag{11}$$

The Cauchy stress σ in Eq. (10)₁ is defined as

$$\sigma = \frac{\partial \psi^{e}}{\partial \epsilon^{e}} = g(d) \left(\lambda \left\langle \operatorname{tr} \varepsilon^{e} \right\rangle_{+} \mathbf{1} + 2\mu \varepsilon^{e+} \right) + \left(\lambda \left\langle \operatorname{tr} \varepsilon^{e} \right\rangle_{-} \mathbf{1} + 2\mu \varepsilon^{e-} \right). \tag{12}$$

And the elastic strain is expressed as

$$\varepsilon^{e} = \varepsilon - \varepsilon^{j} = \nabla u - n^{\Gamma_{\beta}} \otimes^{s} v \gamma_{\beta} (\beta, \nabla \beta).$$
(13)

By considering variations in the phase field, displacement, and displacement jump, we derive the weak form as follows

$$\int_{\Omega} \left\{ \left(2\mathcal{H} + \frac{g_c}{\ell} \right) d\delta d + g_c \ell \nabla d \cdot \nabla d \left(\delta d \right) \right\} d\Omega = \int_{\Omega} 2\delta \mathcal{H} dd\Omega, \tag{14a}$$

$$\int_{\Omega} \sigma \colon \varepsilon^{e} \left(\delta u \right) d\Omega = \int_{\partial \Omega_{r}} \overline{F} \cdot \delta u d\Gamma, \tag{14b}$$

$$\int_{\Omega} \left\{ \gamma_{\beta} \left(\boldsymbol{t} \left(\boldsymbol{v}, \kappa \right) - \sigma \colon \varepsilon^{j} \left(\delta \boldsymbol{v} \right) \right) - \alpha \frac{\partial \boldsymbol{v}}{\partial x_{n}} \cdot \frac{\partial \delta \boldsymbol{v}}{\partial x_{n}} \right\} d\Omega - \int_{\partial \Gamma_{\beta}} \frac{\partial \boldsymbol{v}}{\partial x_{n}} \delta \boldsymbol{v} d\Gamma = 0.$$
 (14c)

Eqs. (9)–(10) are solved using a standard finite element procedure with a staggered scheme at each time step or load increment. More theoretical and practical details are available in [10].

3. EFFECT OF MATRIX-AGGREGATE INTERFACE ON EFFECTIVE MEDIUM

In this section, we analyze the effect of the matrix-aggregate interface on the effective medium properties, considering both elastic and damage behavior. The model consists of a circular aggregate with a radius R embedded in a square matrix domain measuring 10×10 mm. A uniform displacement is applied along the Y-direction at the top edge of the specimen, while the bottom edge is fixed to restrict any displacement in the Y-direction, as depicted in Fig. 1. Plane strain is assumed. The volume fraction of aggregate varies from 0 to 60% by adjusting its radius. The specimen is meshed with triangular elements, with a minimum element size $h_{\min} = 0.25$ mm and $h_{\rm max} = 0.5$ mm is the maximum size in the zone where no crack is expected. All simula-

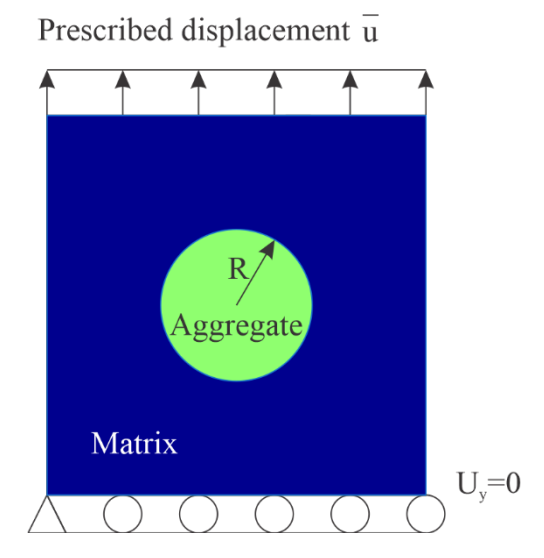


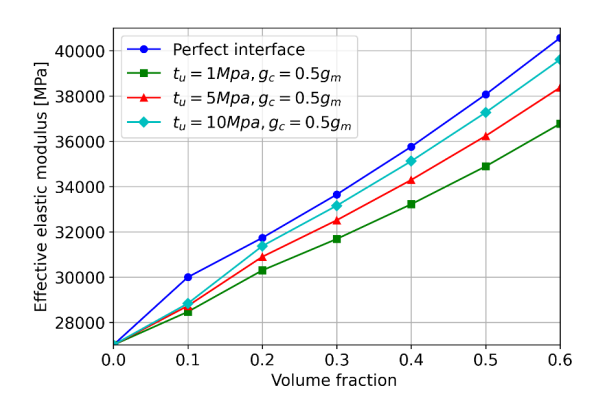
Fig. 1. Geometry and boundary condition

tions were performed on a Dell machine with an Intel(R) Xeon(R) CPU @ 2.4 GHz and 64 GB RAM. Each simulation took approximately 2 hours.

First, the effect of fracture strength on the effective modulus of the specimen is represented in Fig. 2. The fracture energy of the interface is set to 0.5 times the fracture energy of the matrix. Three values of fracture strength are considered: $t_u = 1$ MPa, 5 MPa, and 10 MPa. For all volume fractions, specimens with a perfect interface exhibit a higher effective elastic modulus compared to those with an imperfect interface. For the imperfect interface, increasing fracture strength enhances the effective elastic modulus. At a volume fraction of 0.1, the difference in effective elastic modulus is negligible, but it becomes more pronounced as the volume fraction increases.

The influence of fracture energy on the effective elastic modulus is illustrated in Fig. 3. The fracture strength is fixed at 5 MPa, while three fracture energy are analyzed: $g_c = 0.5g_m$, $g_c = g_m$, and $g_c = 2g_m$. Similarly, for all volume fractions, specimens with a perfect interface exhibit a higher effective elastic modulus compared to those with an imperfect interface. However, contrary to the fracture strength, an increase in fracture energy leads to a decrease in the effective elastic modulus of the specimen. As observed

with fracture strength, specimens with a perfect interface consistently exhibit a higher effective elastic modulus than those with an imperfect interface. However, unlike fracture strength, increasing the fracture energy leads to a decrease in the effective elastic modulus of the specimen.



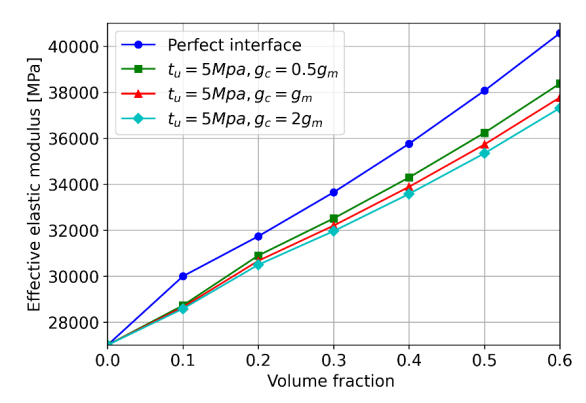


Fig. 2. Effect of fracture strength on the effective elastic modulus

Fig. 3. Effect of fracture energy on the effective elastic modulus

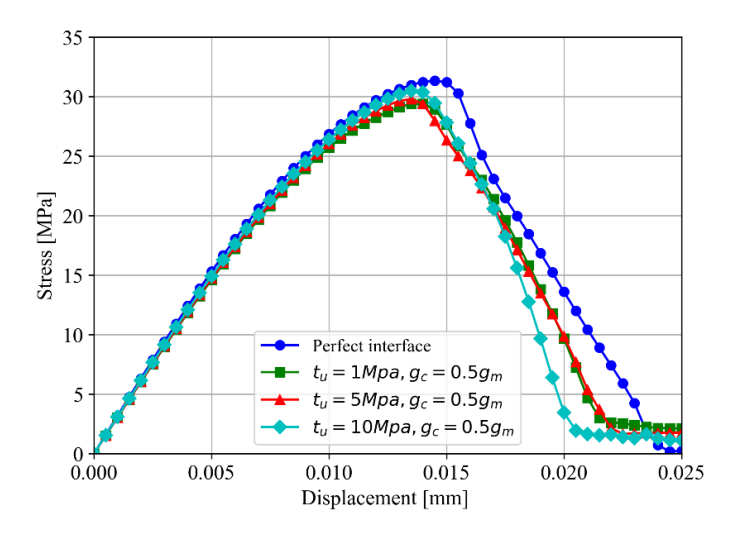


Fig. 4. Stress-displacement curves for different fracture strengths at a volume fraction of 0.2

To illustrate the effect of interface properties on the damage behavior of the specimen, the volume fraction is maintained at 0.2, and the fracture energy of the interface is set to half that of the matrix. Three fracture strength values are examined: $t_u = 1$ MPa, 5 MPa, and 10 MPa, representing progressively stronger interfaces. Fig. 4 presents the stress-displacement curves for a volume fraction of 0.2. The curve for the perfect interface exhibits the highest peak stress, reflecting ideal stress transfer between the matrix

and the aggregate. For imperfect interfaces, increasing the fracture strength results in a higher peak stress, indicating improved stress resistance.

Fig. 5 shows the initiation of cracks for different fracture strengths. For the perfect interface, cracks initiate in the matrix. For the imperfect interface, cracks initiate at the interface between the matrix and the aggregate. Higher fracture strength leads to shorter interfacial cracks, as the stronger interface resists crack propagation more effectively. Fig. 6 illustrates the final crack patterns for all cases. In general, cracks propagate perpendicular to the applied tensile load.

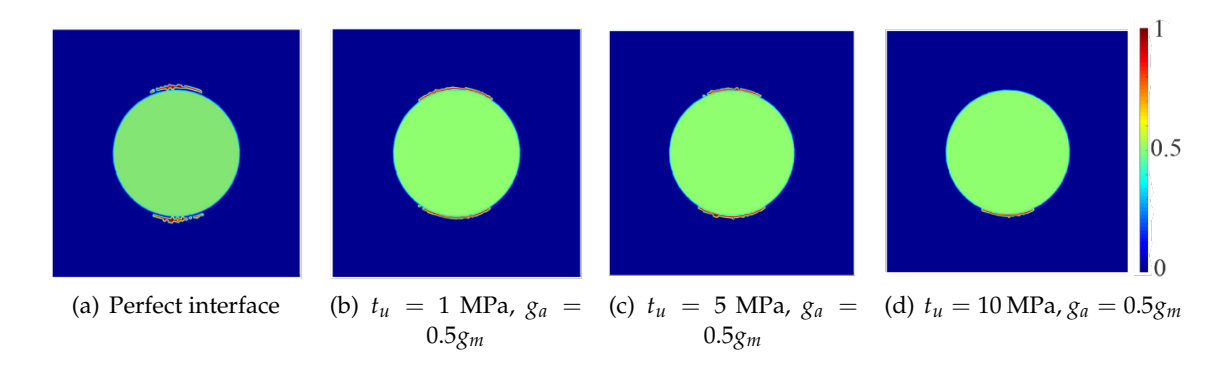


Fig. 5. Crack initiation for different fracture strengths at a volume fraction of 0.2

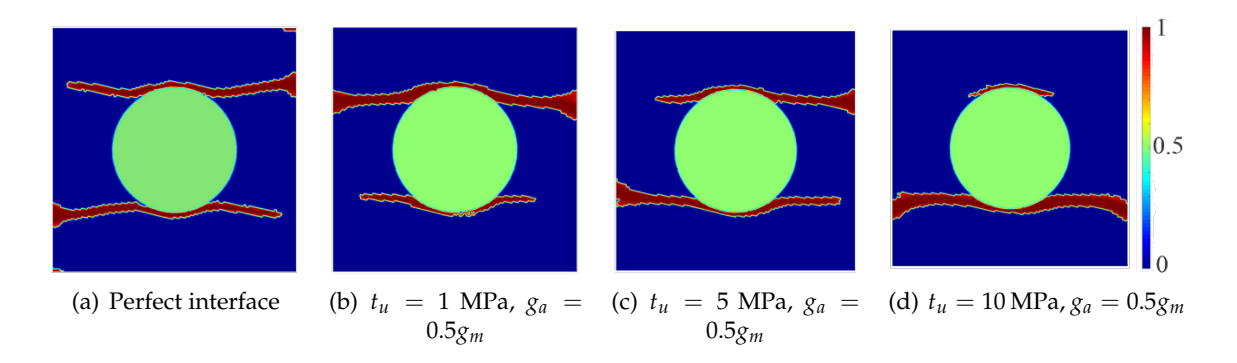


Fig. 6. Crack patterns for different fracture strengths at a volume fraction of 0.2

4. MESO-SCALE MODEL FOR SFRC

This section examines the influence of the interface between the aggregate and the matrix on the flexural behavior of Steel Fiber Reinforced Concrete (SFRC) through a three-point bending test model. The geometry and boundary conditions of the test are illustrated in Fig. 7. The experimental and simulation results were previously conducted

by Bitencourt (2019) [12] and Ribero (2023) [13]. To investigate the effects, calculations were performed under two scenarios: considering and neglecting the imperfect interface between the aggregate and the matrix, while consistently accounting for the imperfect interface between the fiber and the matrix. For demonstration purposes, the interface properties between the aggregate and the matrix are assumed to be identical to those between the fiber and the matrix. The material parameters are detailed in Table 1, while the length scale ℓ is fixed at 0.5 mm.

		Elastic modulus (GPa)	Poisson ratio	Fracture energy (kN/mm)	Interface strength (GPa)	Volume fraction (%)
Three point bending test	Aggregate	47	0.2	1.2e-5	-	35
	Cement mortar	20	0.2	3e-6	-	64.25
	Steel	210	0.3	1e-2	-	0.25
	Interface	-	-		1e-3	-

Table 1. The material parameters in three bending test

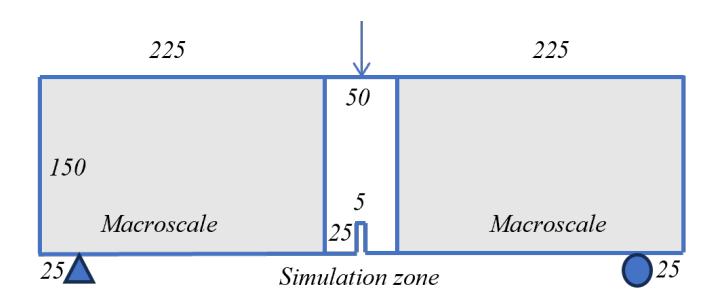


Fig. 7. Geometry and boundary conditions of the three-point bending test

Fig. 8 compares the stress-displacement curves for different approaches. The numerical simulation results are in good agreement with the experimental results. It is observed that when only the interface between the fiber and matrix is assumed to be imperfect, the present model closely matches both the experimental data and the numerical models from the literature. However, when all interfaces are assumed to be imperfect, both the peak load and stiffness of the specimen decrease. This behavior is consistent with the results observed in the single aggregate case discussed in the previous section. In general, the interface represents the weakest point of the specimen. When both interfaces are considered imperfect, cracks form more easily, resulting in a reduction in both the specimen's stiffness and peak load.

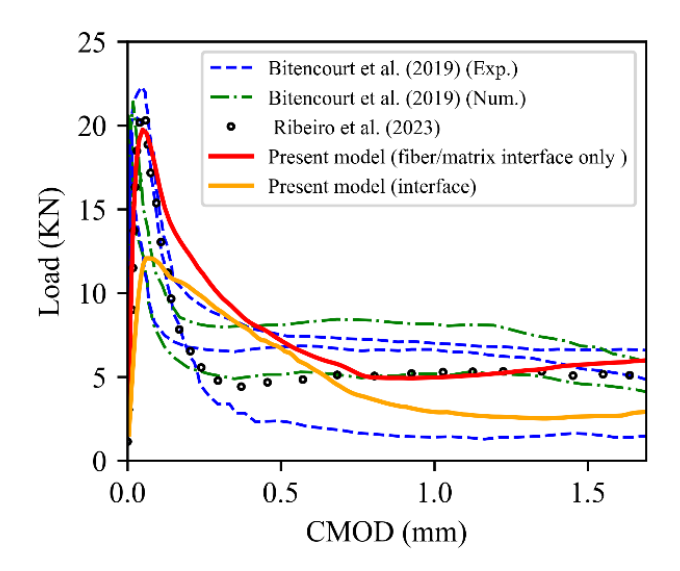


Fig. 8. Comparison of stress-displacement curves for different approaches

5. CONCLUSION

This paper examines the impact of the interface between aggregate and mortar on the damage behavior of Steel Fiber Reinforced Concrete (SFRC). The damage behavior of SFRC is modeled using a cohesive fracture approach enhanced with the phase field method. The model's performance is evaluated through two examples: (i) a circular aggregate embedded in a homogeneous matrix and (ii) a three-point bending test of SFRC at the mesoscale level. Based on the numerical results from the proposed model, the following conclusions can be drawn:

- A perfect interface between the aggregate and mortar matrix results in a higher effective modulus of the medium. When the fracture energy remains constant, a higher fracture strength enhances the effective elastic modulus. Conversely, when the fracture strength is constant, an increase in fracture energy reduces the effective elastic modulus of the specimen;
- Regarding damage behavior, fracture strength affects the localization of crack initiation. With a perfect interface, cracks initiate in the matrix. Conversely, with an imperfect interface, cracks initiate at the interface between the aggregate and mortar matrix. Higher fracture strength results in shorter interfacial cracks;
- When only considering the interface between fiber and matrix, the proposed model aligns well with experimental results and previous numerical models. However, when both the fiber/matrix and aggregate/matrix interfaces are taken into account, the proposed model exhibits lower stiffness and lower peak load.

In this paper, the cohesive law is considered only at the interface between phases, while the behavior of steel is assumed to be elastic. In future research, the proposed model will be enhanced by incorporating factors such as the cohesive law throughout the entire medium and the plastic behavior of steel fibers to more accurately simulate the behavior of SFRC.

DECLARATION OF COMPETING INTEREST

The authors declare that they have no known competing financial interests or personal relationships that could have appeared to influence the work reported in this paper.

ACKNOWLEDGMENT

This research is funded by Vietnam National Foundation for Science and Technology Development (NAFOSTED) under grant number 107.02-2023.15.

REFERENCES

- [1] A. Bentur and S. Mindess. *Fibre reinforced cementitious composites*, Modern Concrete Technology Series. CRC Press, (2006). https://doi.org/10.1201/9781482267747.
- [2] L. A. Le, G. D. Nguyen, H. H. Bui, A. H. Sheikh, and A. Kotousov. Incorporation of micro-cracking and fibre bridging mechanisms in constitutive modelling of fibre reinforced concrete. *Journal of the Mechanics and Physics of Solids*, **133**, (2019). https://doi.org/10.1016/j.jmps.2019.103732.
- [3] A. E. Naaman and H. W. Reinhardt. Proposed classification of HPFRC composites based on their tensile response. *Materials and Structures*, **39**, (2006), pp. 547–555. https://doi.org/10.1617/s11527-006-9103-2.
- [4] Y. Chen, G. Cen, and Y. Cui. Comparative analysis on the anti-wheel impact performance of steel fiber and reticular polypropylene synthetic fiber reinforced airport pavement concrete under elevated temperature aging environment. *Construction and Building Materials*, 192, (2018), pp. 818–835. https://doi.org/10.1016/j.conbuildmat.2018.10.175.
- [5] B. Belletti, R. Cerioni, A. Meda, and G. Plizzari. Design aspects on steel fiber-reinforced concrete pavements. *Journal of Materials in Civil Engineering*, **20**, (2008), pp. 599–607. https://doi.org/10.1061/(asce)0899-1561(2008)20:9(599).
- [6] Y. Zhang and D. Dias-da Costa. Seismic vulnerability of multi-span continuous girder bridges with steel fibre reinforced concrete columns. *Engineering Structures*, **150**, (2017), pp. 451–464. https://doi.org/10.1016/j.engstruct.2017.07.053.
- [7] A. Conforti, G. Tiberti, G. A. Plizzari, A. Caratelli, and A. Meda. Precast tunnel segments reinforced by macro-synthetic fibers. *Tunnelling and Underground Space Technology*, **63**, (2017), pp. 1–11. https://doi.org/10.1016/j.tust.2016.12.005.
- [8] V. M. C. F. Cunha, J. A. O. Barros, and J. M. Sena-Cruz. A finite element model with discrete embedded elements for fibre reinforced composites. *Computers & Structures*, **94–95**, (2012), pp. 22–33. https://doi.org/10.1016/j.compstruc.2011.12.005.

- [9] F. K. F. Radtke, A. Simone, and L. J. Sluys. A computational model for failure analysis of fibre reinforced concrete with discrete treatment of fibres. *Engineering Fracture Mechanics*, 77, (2010), pp. 597–620. https://doi.org/10.1016/j.engfracmech.2009.11.014.
- [10] H.-Q. Nguyen, G.-K. Le, B.-A. Le, and B.-V. Tran. A cohesive fracture-enhanced phase-field approach for modeling the damage behavior of steel fiber-reinforced concrete. *Engineering Fracture Mechanics*, **311**, (2024). https://doi.org/10.1016/j.engfracmech.2024.110603.
- [11] C. Miehe, M. Hofacker, and F. Welschinger. A phase field model for rate-independent crack propagation: Robust algorithmic implementation based on operator splits. *Computer Methods in Applied Mechanics and Engineering*, **199**, (2010), pp. 2765–2778. https://doi.org/10.1016/j.cma.2010.04.011.
- [12] L. A. G. Bitencourt, O. L. Manzoli, T. N. Bittencourt, and F. J. Vecchio. Numerical modeling of steel fiber reinforced concrete with a discrete and explicit representation of steel fibers. *International Journal of Solids and Structures*, **159**, (2019), pp. 171–190. https://doi.org/10.1016/j.ijsolstr.2018.09.028.
- [13] L. Felipe dos Santos Ribeiro, C. Mejia, and D. Roehl. Multiphase and mesoscale analysis of the mechanical behavior of fiber reinforced concrete. *Theoretical and Applied Fracture Mechanics*, 125, (2023). https://doi.org/10.1016/j.tafmec.2023.103929.